Solar Phys (2011) 271:91–110
DOI 10.1007/s11207-011-9785-7

Simulation of the Unusual Solar Minimum with 3D SIP-CESE MHD Model by Comparison with Multi-Satellite Observations

Liping Yang · Xueshang Feng · Changqing Xiang · Shaohua Zhang · S.T. Wu

Received: 5 January 2011 / Accepted: 29 April 2011 / Published online: 15 June 2011

Abstract The observations both near the Sun and in the heliosphere during the activity minimum between solar cycles 23 and 24 exhibit different phenomena from those typical of the previous solar minima. In this paper, we have chosen Carrington rotation 2070 in 2008 to investigate the properties of the background solar wind by using the three-dimensional (3D) Solar–InterPlanetary Conservation Element/Solution Element Magnetohydrodynamic (MHD) model. We also study the effects of polar magnetic fields on the characteristics of the solar corona and the solar wind by conducting simulations with an axisymmetric polar flux added to the observed magnetic field. The numerical results are compared with the observations from multiple satellites, such as the *Solar and Heliospheric Observatory* (SOHO), *Ulysses*, *Solar Terrestrial Relations Observatory* (STEREO), *Wind* and the *Advanced Composition Explorer* (ACE). The comparison demonstrates that the first simulation with the observed magnetic fields reproduces some observed peculiarities near the Sun, such as relatively small polar coronal holes, the presence of mid- and low-latitude holes, a tilted and warped current sheet, and the broad multiple streamers. The numerical results also capture the inconsistency between the locus of the minimum wind speed and the location of the heliospheric current sheet, and predict slightly slower and cooler polar streams with a relatively smaller latitudinal width, broad low-latitude intermediate-speed streams, and globally weak magnetic field and low density in the heliosphere. The second simulation with strengthened polar fields indicates that the weak polar fields in the current minimum play a crucial role in determining the states of the corona and the solar wind.

Keywords Numerical MHD method · Polar field · Solar minimum · Solar wind simulation

L. Yang · X. Feng (✉) · C. Xiang · S. Zhang
SIGMA Weather Group, State Key Laboratory for Space Weather, Center for Space Science and Applied Research, Chinese Academy of Sciences, Beijing 100190, China
e-mail: fengx@spaceweather.ac.cn

L. Yang · S. Zhang
College of Earth Sciences, Graduate University of Chinese Academy of Sciences, Beijing 100049, China

S.T. Wu
CSPAR, The University of Alabama in Huntsville, Huntsville, AL 35899, USA

1. Introduction

Unlike the past solar minima since the dawn of the space age, the minimum of activity between solar cycles (SC) 23 and 24 (briefly called the current minimum in the following) had many unusual properties. The sunspot numbers were at their lowest in 75 years (Gibson *et al.*, 2009) and over 200 spotless days in 2008 were the highest recorded in the last 50 years (Tokumaru *et al.*, 2009). SC 24 started much later than expected, which left behind a long quiet minimum unlike any other one in the past 100 years (Hathaway and Rightmire, 2010). Wang, Robbrecht, and Sheeley (2009) investigated the solar polar field during SC 23 by using the magnetograph data from both the Mount Wilson Observatory (MWO) and the Wilcox Solar Observatory (WSO) and found that the arithmetic mean polar field strength was only $\approx 4-5$ gauss (G) during the 2008 minimum while it ranged between about 6 and 9 G during the 1976, 1986, and 1996 sunspot minima.

At the same time, the corona did not show the characteristics of well-formed polar coronal holes (PCHs) associated with typical solar minima for a long time, but only presented quite weak, asymmetric PCHs, which floated around the solar disk (in longitude) as the Sun rotated (Schatten, 2005). With the use of the automated detection of EUV PCHs, Kirk and Pesnell (2009) observed that the north and south polar hole areas were about 15% smaller in 2007 than those at the beginning of SC 23. Besides, Abramenko *et al.* (2010) found that the area occupied by mid- and low-latitude coronal holes (MLCHs), which lied between $\pm 40^\circ$ latitudes around the solar equator, was larger in the minimum of SC 23/24 than that in the corresponding phase of SC 22/23 and that the most long-lived MLCH existed for 27 rotations. Other distinct features include multiple white-light coronal streamers which were not confined to low latitudes, and a peculiar current sheet (CS) derived from the potential-field source-surface (PFSS) model, which retained a significantly higher inclination than that typically seen around most solar minima (de Toma and Arge, 2010).

Measurements from the third fast-latitude scan of *Ulysses* (Wenzel *et al.*, 1992) also revealed a quite different solar wind condition during the current minimum. The fast solar wind emanating from large PCHs was 3% slower, 17% less dense and cooler than that during the preceding one (McComas *et al.*, 2008; Issautier *et al.*, 2008). The interplanetary magnetic field (IMF) measurements from *Ulysses* indicated that the average radial component of IMF was only about two-thirds of that measured during the preceding one, which was possibly due to less open solar fluxes in the PCHs (Smith and Balogh, 2008). While the heliosphere generally returned to a more ordered state and the sunspot numbers were lower, *Ulysses* observed more variable structures of the solar wind and more interplanetary coronal mass ejections than during its first fast latitudinal scan. McComas *et al.* (2006) suggested that the difference probably resulted from both recurrent high-speed streams persisting in the ecliptic and a complicated heliospheric current sheet (HCS) including a large inclination to the solar equator and a significant non-planarity with respect to the belt of low-speed winds.

The interplanetary scintillation (IPS) observations have revealed that the solar wind structure in the current minimum greatly differed from that observed during the previous two minima (Tokumaru *et al.*, 2009). The fast solar wind emanated not only from the poles but also from the equatorial region and the poleward boundary of the slow wind could extend to 30° north and south. Tokumaru, Kojima, and Fujiki (2010) also demonstrated a distinct decrease of high-speed wind at high latitudes and a marked growth of the fast- and intermediate-speed wind at low latitudes during the late phase of SC 23, which was supported by measurements from the *Advanced Composition Explorer* (ACE, Stone *et al.*, 1998). Toward the 2008 minimum, the occurrence rate of the wind speed at about 600 km s^{-1} substantially increased, and

its peak was almost comparable to that at about 400 km s^{-1}. The OMNI data (Cooper *et al.*, 1995) revealed the properties of the solar wind near the Earth in the current minimum, which are different from those in the last minimum. Lee *et al.* (2009) found both the IMF magnitude and density were 30% lower, the momentum flux was 38% lower, and the velocity remained almost unchanged, which was consistent with the *Ulysses* off-ecliptic observations reported by McComas *et al.* (2008) and Smith and Balogh (2008). Gibson *et al.* (2009) statistically studied the solar wind parameters in nine solar rotations around the Whole Sun Month (WSM, 10 August to 8 September 1996) and the Whole Heliosphere Interval (WHI, 20 March to 16 April 2008) and demonstrated that, during the WHI period, IMF strength near the Earth decreased by 15% and density decreased by 45%. However, the solar wind velocity actually increased by 13% on average.

Carrington rotation (CR) 2070 began on 13 May 2008 and ended on 9 June 2008. According to the research on low-latitude coronal holes at the minimum of SC 23 by Abramenko *et al.* (2010), the dipole component of the power spectrum of the photospheric magnetic field during CR 2070 was about 8×10^3 μT^2 and the sum of the other multi-poles was 4×10^4 μT^2. The areas of MLCHs occupied about 0.02% of the solar disk, determined from Fe XV 284 Å synoptic maps observed by the *Solar and Heliospheric Observatory* (SOHO)/Extreme ultraviolet Imaging Telescope (EIT, Delaboudinière *et al.*, 1995). The harmonic power spectra and the area of MLCHs were roughly the same as the corresponding averages from CR 2060 to CR 2077. Additionally, the solar wind observed by IPS in this CR exhibited a significantly non-dipolar structure with polar and equatorial fast streams and slow streams in between (Tokumaru *et al.*, 2009). Therefore, we choose CR 2070 in 2008 to study the characteristics of the background solar wind, since 2008 is unusual and a very interesting part of the current minimum.

These uncommon properties during the current minimum provide us with an excellent opportunity to gain better insight into the structures of the solar wind and their relationship with the magnetic field through numerical MHD simulations, which have been widely used in the study of background solar wind and solar transients (Linker *et al.*, 1999; Endeve, Leer, and Holzer, 2003; Riley *et al.*, 2006; Lepri *et al.*, 2008; Kleimann *et al.*, 2009; Kataoka *et al.*, 2009). In the present study, we will use the three-dimensional (3D) Solar–InterPlanetary Conservation Element/Solution Element (SIP-CESE) Magnetohydrodynamic (MHD) model (Feng, Zhou, and Wu, 2007; Feng *et al.*, 2010) to numerically investigate the peculiarities of the current minimum and to explore their relationship with the polar magnetic fields on the solar surface. In order to achieve this, we have chosen CR 2070 as the simulation time interval and we will compare the numerical results with observations from multiple satellites, such as SOHO, *Ulysses*, *Solar Terrestrial Relations Observatory* (STEREO, Kaiser *et al.*, 2008), *Wind* (Lepping *et al.*, 1995) and ACE. In addition, we will conduct two case studies to probe the effects of the polar magnetic fields: one is the run with the observed photospheric magnetic field of CR 2070 as initial magnetic input and the other is obtained with the strengthened radial polar fields. A concise description of the 3D SIP-CESE MHD model will be provided in Section 2. The simulation results will be presented in Section 3, and in the last section the conclusions and discussions will be given.

2. The 3D SIP-CESE MHD Model

The details of the 3D SIP-CESE MHD model were described in Feng, Zhou, and Wu (2007) and Feng *et al.* (2010). In this section only the basic features and modifications specific to

this study are given. By splitting the magnetic field, the solar–interplanetary MHD system can be written as

$$\frac{\partial \rho}{\partial t} + \nabla \cdot \rho \mathbf{u} = 0,$$

$$\frac{\partial \rho \mathbf{u}}{\partial t} + \nabla \cdot \left[\rho \mathbf{u}\mathbf{u} + \mathbf{I}\left(p + \frac{1}{2}\mathbf{B}_1^2 + \mathbf{B}_1 \cdot \mathbf{B}_0 \right) - \mathbf{B}_1\mathbf{B}_1 - \mathbf{B}_1\mathbf{B}_0 - \mathbf{B}_0\mathbf{B}_1 \right] = \mathbf{j}_0 \times \mathbf{B}_0 + \rho\big[\mathbf{g} - \boldsymbol{\Omega} \times (\boldsymbol{\Omega} \times \mathbf{r})\big] - 2\rho\boldsymbol{\Omega} \times \mathbf{u},$$

$$\frac{\partial e_1}{\partial t} + \nabla \cdot \left[\mathbf{u}\left(e_1 + p + \frac{1}{2}\mathbf{B}_1^2 + \mathbf{B}_1 \cdot \mathbf{B}_0 \right) - (\mathbf{u} \cdot \mathbf{B}_1)(\mathbf{B}_1 + \mathbf{B}_0) \right] = -\mathbf{B}_1 \cdot \frac{\partial \mathbf{B}_0}{\partial t} + \mathbf{E} \cdot \mathbf{j}_0 + \rho\mathbf{u} \cdot \big[\mathbf{g} - \boldsymbol{\Omega} \times (\boldsymbol{\Omega} \times \mathbf{r})\big] + Q_\mathrm{e},$$

$$\frac{\partial \mathbf{B}_1}{\partial t} + \nabla \cdot (\mathbf{u}\mathbf{B} - \mathbf{B}\mathbf{u}) = -\frac{\partial \mathbf{B}_0}{\partial t},$$

where

$$\mathbf{E} = \mathbf{u} \times \mathbf{B}, \qquad \mathbf{j}_0 = \nabla \times \mathbf{B}_0,$$

and

$$e_1 = \frac{1}{2}\rho\mathbf{u}^2 + \frac{p}{\gamma - 1} + \frac{1}{2}\mathbf{B}_1^2,$$

which corresponds to the modified total energy density consisting of the kinetic energy density, thermal energy density, and magnetic energy density written in terms of $\mathbf{B}_1$. Here, ρ is the mass density; $\mathbf{u} = (u, v, w)$ are the velocity components in the x, y, and z directions; p is the thermal pressure; $\mathbf{B}$, $\mathbf{B}_0$, and $\mathbf{B}_1$ denote the total magnetic field, the potential magnetic field and its perturbed component such as $\mathbf{B} = \mathbf{B}_0 + \mathbf{B}_1$. Variables t and $\mathbf{r}$ are the time and the position vector whose origin is at the center of the Sun; $\mathbf{g} = -(GM/r^3)\mathbf{r}$ is the solar gravitational force, $\boldsymbol{\Omega}$ is the angular velocity of solar rotation and γ is the ratio of specific heats. Q_e stands for the energy-source term, which is responsible for heating and acceleration of the solar wind.

The equations are normalized by the characteristic values ρ_s, a_0, $\rho_\mathrm{s}a_0^2$, $\sqrt{\rho_\mathrm{s}a_0^2}$, R_s, R_s/a_0, and a_0^2/R_s, where ρ_s and a_0 are the density and ion-acoustic wave speed at the solar surface. A factor of $1/\sqrt{\mu}$ has been absorbed into the definition of $\mathbf{B}$. For $\mathbf{B}_0$ constant in time and force free, many terms about $\mathbf{B}_0$ in the right hand side can vanish. In the present study, the solar rotation is considered with angular velocity $|\boldsymbol{\Omega}| = 2\pi/27.2753$ radian day^{-1} and γ is set to be 1.5. Q_e is given as follows:

$$Q_\mathrm{e} = Q_1 \exp(-R/L_{Q_1}) + Q_2(R-1)\exp(-R/L_{Q_2}) + \nabla\left(\xi T^{\frac{5}{2}} \frac{\nabla T \cdot \mathbf{B}}{B^2} \right) \cdot \mathbf{B},$$

where $Q_2 = Q_0 C_\mathrm{a}$, $C_\mathrm{a} = C_\mathrm{a}'/\max(C_\mathrm{a}')$ with $C_\mathrm{a}' = \frac{(5.8 - 1.6e^{[1-(\theta_\mathrm{b}/8.5)^3]})^{3.5}}{(1+f_\mathrm{s})^{2/7}}$ (Feng *et al.*, 2010). Q_1 and Q_0 in this paper are given as 3×10^{-9} J m^{-3} s^{-1} and 4.5×10^{-7} J m^{-3} s^{-1} respectively and $\xi = 5\varepsilon_\mathrm{p} = 1.6 \times 10^{-12}$ J m^{-1} s^{-1} K$^{-7/2}$. ε_p is the proton conductivity, equal to 3.2×10^{-13} J m^{-1} s^{-1} K$^{-7/2}$ as given by Braginskii (1965). L_{Q_1} and L_{Q_2} are set to be 1 and 0.8 R_s. Here, f_s is the areal expansion factor of the magnetic flux tubes and θ_b is the

minimum angular separation at the photosphere between an open field foot point and its nearest coronal hole boundary. Similar empirical functions like C'_a with various free parameters have been employed to derive the solar wind speed near the Sun (Arge *et al.*, 2004; Owens *et al.*, 2005). The expansion factor (Wang and Sheeley, 1990) reads $f_s = (\frac{R_s}{r})^2 \frac{B_{R_s}}{B_r}$ where R_s and r are the solar radius and the distance from the solar center, and B_{R_s} and B_r are magnetic field strengths at the solar surface and at r, respectively. The use of both f_s and θ_b is motivated by the observation that there exists a close relationship between the solar wind velocity and the inverse of the expansion factor (Wang and Sheeley, 1990) and the angular distance θ_b distinguishes the high-speed solar winds from the low-speed solar wind (high-speed stream originating from the center of an open field region has large θ_b and low-speed stream from the hole boundary has a small θ_b). Conventionally, the PFSS model (Luhmann *et al.*, 2002; Zhao *et al.*, 2006; Hu *et al.*, 2008; Feng *et al.*, 2010) is employed to determine the expansion factor f_s and the value of θ_b and it chooses the source surface at 2.5 R_s. However, we will provide f_s and θ_b with additional meanings to allow them to have a 3-D distribution from the solar surface at 1 R_s to the source surface at 2.5 R_s. For details, refer to Feng *et al.* (2010). By the way, Nakamizo *et al.* (2009) considered the expansion factor f_s in the heating source terms for the solar wind study.

We will use the six-component grid system as adopted by Feng *et al.* (2010) to avoid the singularity and mesh convergence near the poles and to conveniently carry out the parallel implementation. The numerical dissipation induced by Courant–Friedrichs–Levy number disparity is reduced by a Courant-number insensitive method, and the fast multigrid Poisson solver is employed to remove the $\nabla \cdot \mathbf{B}$ error. At last, we will use multiple time stepping to speed up the computation and enhance the accuracy of numerical solution.

The calculation is performed between 1 R_s (*i.e.*, the base of the corona) and 247 R_s. At the lower boundary, based on the observed line-of-sight measurements of the photospheric magnetic field from WSO at Stanford University, we specify the radial component of the magnetic field. The initial temperature and number density on the solar surface are set to be 1.3×10^6 K and 1.5×10^8 cm^{-3}, respectively. We combine the methods of the projected normal characteristic boundary condition and the technique of limiting mass flux through the solar surface to adjust the distributions of temperature, density, and speed on the bottom boundary (Feng *et al.*, 2010). Then, the potential magnetic field based on the photospheric magnetic field of CR 2070 and Parker solar wind solution are employed as initial inputs to our code, which is advanced in the time-relaxation method to achieve a dynamic, steady-state equilibrium. The numerical results are given in the following section.

3. Numerical Results

3.1. Results with the Observed Photospheric Magnetic Field

Figure 1 displays the synoptic maps of the MHD solution and observations near the Sun. Figures 1(a) and (b) show the distributions of the simulated radial magnetic field B_r and the observation of STEREO-A Sun Earth Connection Coronal and Heliospheric Investigation (SECCHI) EUVI 195 Å for CR 2070 on the solar surface, respectively. In Figure 1(a), the orange and purple lines represent the derived boundaries of coronal holes from the MHD and PFSS models, which are produced by separating the regions where the field lines return to the Sun from the regions where the field lines reach the outer boundaries at 5 R_s (Feng *et al.*, 2010). Figures 1(c) – (h) show the synoptic maps at 2.5 R_s. Figures 1(c), (e) and (g) correspond to the simulated B_r, number density N, and radial speed v_r. Figure 1(d)

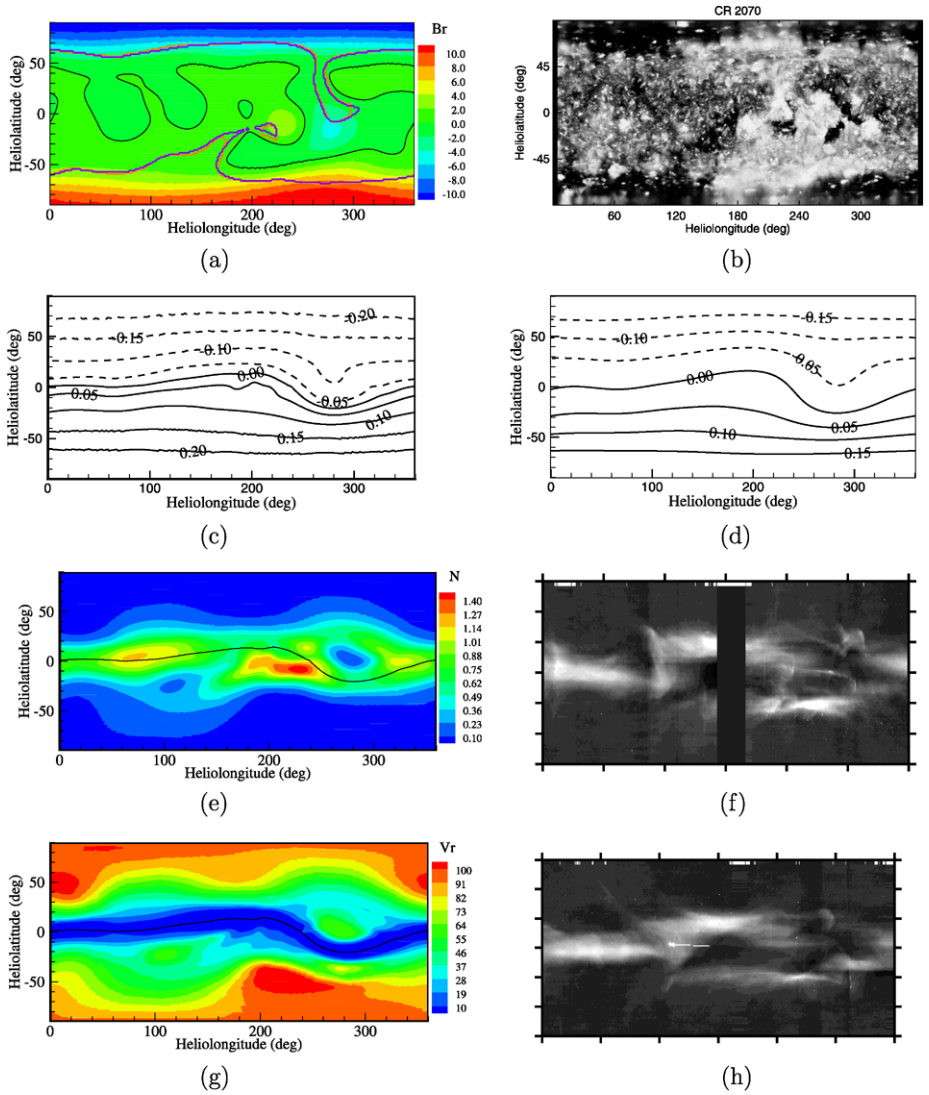

Figure 1 Synoptic maps at 1 R_S. (a) The simulated radial magnetic field B_r (unit: G), (b) STEREO-A SECCHI EUVI 195 Å observation, (c, d) contour maps of B_r (unit: gauss (G)) at 2.5 R_S from MHD (c) and PFSS (d) models, (e) the simulated number density N (unit: 10^6 cm^{-3}) and (g) radial speed v_r (unit: km s^{-1}). Panels (f) and (h) show the white-light polarized brightness at the east (f) and west (h) limbs from SOHO/LASCO C2. In panels (a), (e) and (g), the black lines denote the magnetic neutral lines.

shows the contours of B_r from the PFSS model. Figures 1(f) and (h) show the synthesized white-light polarized brightness (pB) at the east and west limbs constructed by extracting from successive Large Angle Spectrometric Coronograph (LASCO) C2 images a slice of east or west limb data centered at $r = 2.5$ R_s and assembling the strips into time-reversed sequences.

Figures 1(a) and (b) demonstrate that the shapes and distributions of coronal holes from the MHD solution are roughly consistent with STEREO/EUVI observation. Both the MHD

and PFSS models display that the northern PCH extends to a latitude (θ) of about $-10°$ at a longitude (ϕ) of 280° and the southern one to $\theta = -20°$ at $\phi = 170°$, while in the EUVI observation, they reached $\theta = -10°$ at $\phi = 280°$ and $\theta = 0°$ at $\phi = 180°$, respectively. Both models also produce the isolated MLCH centering at $\theta = -15°$ and $\phi = 225°$, whose polarity is the same as the southern PCH. However, neither the MHD simulation nor the PFSS model yields the one centered at $\theta = -25°$ and $\phi = 170°$ in the EUVI observation. In addition, the extended coronal holes and isolated MLCH from the PFSS model are a little larger than those from the MHD model, but a little smaller than those from the EUVI observation. The median of the equatorward boundaries for both northern and southern PCHs is at about $\theta = 63°$ for the MHD model. In CR 1911 it was at about $\theta = 58°$ according to Feng *et al.* (2010). Therefore, the simulated area of PCHs in CR 2070 shrinks relative to that of CR 1911, which is consistent with the statistical results from the PFSS model (Wang, Robbrecht, and Sheeley, 2009) and the observation from EIT/SOHO (Kirk and Pesnell, 2009).

Comparison between Figures 1(c) and (d) indicates that the magnetic neutral lines (MNL) are similar in the MHD and PFSS models. The MNLs from both models have a peak at about $\phi = 200°$ and a trough at $\phi = 270°$, while the MNL between the peak and the trough from the PFSS model is steeper than that from the MHD model, which indicates the presence of the high tilting and warping of the MNL and also the curving of the streamer belt during this period. The peak and the trough of the MNL are just next to the southern and northern extended coronal holes. Figures 1(e) and (g) show that the MNL was surrounded by regions of high density and low-speed winds, which is in agreement with the observational study made by Wang *et al.* (1997) and Wang, Lean, and Sheeley (2000). We can see that the relatively broad high-density structures were located around the peak and the trough of the MNL, while in other longitudes existed the high-density regions of 30° latitudinal width. This is roughly consistent with the distribution of the *pB* enhanced regions observed by LASCO/C2, as shown in Figures 1(f) and (h). It should be noted that the high-density regions were also present in the vicinity of the northern PCH at $\phi = 300°$.

Figures 2(a) and (b) display the composite observations from the disk to the outer corona on 14 May and on 24 May in CR 2070. Therefore, a continuation of structure from the low to high corona can be seen. The innermost views of the disk and low corona are obtained from the SOHO/EIT images of the He II 304 Å observation. The data on the corona from 1.15 to 2.3 R_s come from Mauna Loa Solar Observatory (MLSO) Mark-IV K-coronameter observation, and the data in the outer fields of view from 2.3 to 6 R_s are from LASCO C2 observations (Morgan, Habbal, and Woo, 2006). Figures 2(c) and (d) display the derived *pB* images from the simulation on the meridional planes at $\phi = 270 - 90°$ and $\phi = 120 - 300°$ from 1.15 to 6 R_s, in which we enhance the *pB* images inside and outside 2.3 R_s separately. Figures 2(e) and (f) show the magnetic field topologies projected onto the meridional planes at $\phi = 270 - 90°$ and $\phi = 120 - 300°$ from 1 to 6 R_s, where the color contours represent B_r on the solar surface and the red lines denote MNL. If we assume little change of the coronal structure within one CR, the meridional planes at $\phi = 270 - 90°$ and $\phi = 120 - 300°$ correspond to the observation on 14 May and 24 May, respectively.

The most significant features in Figure 2 are the presence of multiple streamers, which were not confined to low latitudes. At each of the west limb portions in Figures 2(a) and (c), there exists a single, equatorial "jet" above 3 R_s, so does at the east limb of Figures 2(b) or (d). The "jet" structure is the classic helmet streamer at solar minimum but extends radially farther and covers relatively large latitudes near the Sun. By the way, in the east limb of Figure 2(b), the wide and complex structure results from high-density regions in different longitudes projected onto the sky plane, and the brightest non-radial spike structure is a transient event seen in the movie of LASCO/C2 available from http://alshamess.ifa.hawaii.edu/sdc01/cim_lasco.php.

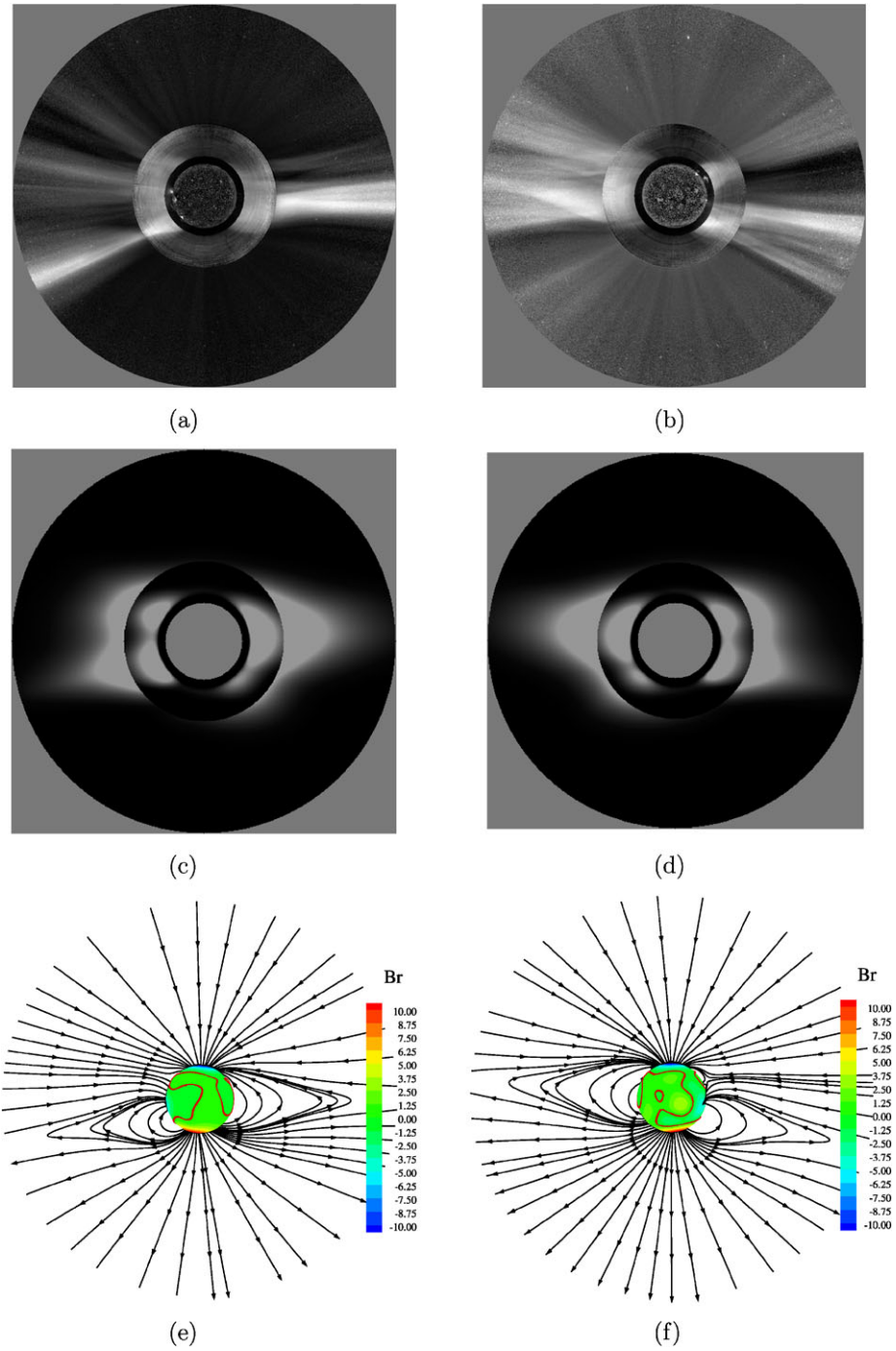

Figure 2 Coronal composite images on (a) 14 May and (b) 24 May and the simulated pB on the meridional planes at (c) $\phi = 270-90^\circ$ and (d) $\phi = 120-300^\circ$ from 1.15 to 6 R_S. Panels (e) and (f) show the magnetic field topology projected onto the meridional planes at (e) $\phi = 270-90^\circ$ and (f) $\phi = 120-300^\circ$ from 1 to 6 R_S, where the color contours represent B_r (unit: G) on the solar surface and the red lines denote MNL.

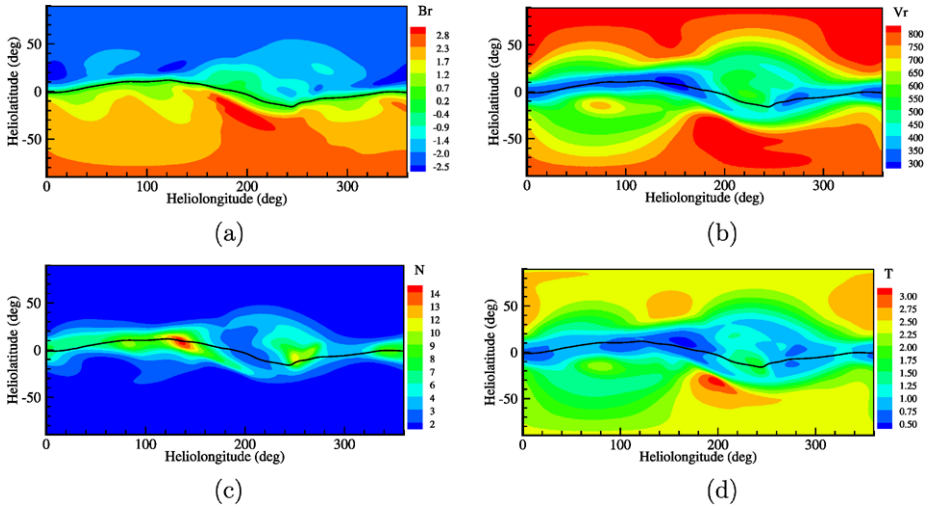

Figure 3 The MHD steady-state solution on the surface at 215 R_s. (a) Contours of radial magnetic field B_r in units of nT, (b) radial velocity v_r in units of km s^{-1}, (c) number density N in units of cm^{-3} and (d) temperature T in units of 10^5 K.

At each of the east-limb regions of Figures 2(a) and (c) and the west-limb regions of Figures 2(b) and (d), there is a highly inclined, radially oriented ray structure in the southern hemisphere and a long, narrow spike configuration in the northern hemisphere. Identified from the simulated magnetic field topologies in Figures 2(e) and (f), the radially oriented ray is associated with the tilted helmet streamer, whose poleward footpoints overlie the polar region at about $\theta = 60°$ and the equatorial footpoints above an active region, which can be identified with NOAA region 10994 according to the SOHO observations and Figures 2(e) and (f). Whereas, the narrow spike configuration results from the high-density region roughly at $\theta = 25°$ and $\phi = 240 - 310°$, which can be seen in Figure 1(e). With the help of the magnetic field line tracing technique, we can confirm that it originates from $\theta = 45°$ at the same longitude on the solar surface. This source region is located above an area of positive polarity that separates two negative-polarity areas, from which the open field lines converge above the area of positive polarity far from the Sun. This configuration in CR 2067 was identified as a pseudo-streamer by Wang, Robbrecht, and Sheeley (2009). Therefore, it was the high-density pseudo-streamer structures that produced the multiple streamers during this period observed by LASCO/C2 and demonstrated by the simulated *pB* results.

The MHD steady-state solution on the surface at 215 R_s is displayed in Figure 3, where panels (a), (b), (c), and (d) correspond to contour maps of radial magnetic field B_r, radial velocity v_r, number density N, and temperature T, respectively. In these maps, the black line denotes the MNL. Figure 3(a) shows that the MNL, also called the HCS at 215 R_s, is not as tilted as that at 2.5 R_s, but it extends northward to $\theta = 10°$ at $\phi = 120°$ and southward to $\theta = -17°$ at $\phi = 245°$. This north–south asymmetry of the locations of the simulated HCS introduces the southward displacement of the HCS relative to the solar equator by about 2°, which can be seen clearly by the fact that there is a slightly stronger radial magnetic field at the south pole than at the north pole. The southward shift of the simulated HCS is compatible with the conclusion drawn by Erdős and Balogh (2010), who analyzed the HCS crossings observed by *Ulysses* during its fast latitudinal scans and showed that the HCS was shifted southward about 2 – 3° in 2007, which was near the se-

lected time interval. Like the southward displacement of the HCS, a small southward shift was present in the streamer belt defined as the high-density low-temperature solar wind around the minimum speed locus. Mursula and Hiltula (2003) also predicted that both the HCS and the streamer belt would be displaced southward during the period. The other distinguishing feature in Figure 3(b) is the inconsistency of the minimum speed locus with HCS, which is most prominent between $\phi = 180°$ and $\phi = 260°$. The inconsistency was found by Mursula, Hiltula, and Zieger (2002), who investigated the effective latitudinal gradients of the solar wind speed in the two magnetic hemispheres around the heliographic equator by analyzing solar wind observations at the Earth's orbit. Compared with the distribution of v_r during the 1996 solar minimum, which was investigated by Feng *et al.* (2010), Figure 3(b) exhibits a distinct decrease of the fast wind areas at high latitudes, a corresponding increase of the slow-intermediate-speed (SIS) wind (< 650 km s^{-1}) areas, and a significant increase of the intermediate-speed wind (> 500 km s^{-1}) areas near the ecliptic, which were also revealed by the IPS observations (Tokumaru *et al.*, 2009; Tokumaru, Kojima, and Fujiki, 2010).

Figure 4 compares the MHD results with the daily averaged data measured by the *Ulysses* satellite (Bame *et al.*, 1992) between $\pm 80°$ latitudes during its third fast latitudinal scan in 2007. The *Ulysses* data are scaled to 1 AU by assuming an r^{-2} falloff for B_r and N, no change for v_r and an $r^{-2(\gamma-1)}$ ($\gamma = 1.46$) variation for T (Usmanov *et al.*, 2000). The two dotted lines in Figure 4(d) give two proton temperatures estimated in two different ways from the observational distributions in the three-dimensional velocity space. The details of the estimation techniques can be seen on the webpage ftp://nssdcftp.gsfc.nasa.gov/spacecraft_data/ulysses/plasma/swoops/ion/swoops_ion_users_guide_update_20030214.txt. These two proton temperatures generally bracket the true temperature.

Figure 4 reveals that the relatively uniform high-speed flows only extended to latitudes equatorward of $\pm 45°$, between which was the rapidly changing SIS solar wind. During the first fast latitudinal scan of *Ulysses* (Usmanov *et al.*, 2000), the SIS solar wind spanned the latitudes of $\pm 30°$. Usmanov *et al.* (2000) also demonstrated that the typical values of the velocity, density, radial magnetic field, and temperature for the high-speed solar wind in the 1996 solar minimum were about 800 km s^{-1}, 3 cm^{-3}, 3 nT, and 3×10^5 K, while they are about 750 km s^{-1}, 2 cm^{-3}, 2 nT, and 2.5×10^5 K in our simulation for CR 2070. So, in the period, the simulated results indicate that the SIS solar wind covered larger latitudes and the fast wind from large PCHs was slightly slower, less dense, cooler, and had less intensified radial magnetic field. This is also consistent with McComas *et al.* (2008) and Smith and Balogh (2008).

Figure 5 compares the simulation results for CR 2070 with the observations from such spacecraft missions as ACE, *Wind* and STEREO. The heliocentric longitudinal separations of the STEREO Ahead(-A) and Behind(-B) spacecraft viewed from the Earth increase approximately 22.5° year^{-1} and the locations of the STEREO spacecraft deviates slightly from 1 AU and the ecliptic plane. Hence we have used the STEREO-A data from 19 May 2008 and the STEREO-B data from 15 May 2008. The OMNI data combine the measurements from ACE, *Wind* and other spacecraft near the L1 point. The OMNI data employed here start from 17 May 2008.

The observations from these spacecraft show that the solar wind in this period was characterized by three broad intermediate-speed streams ($500-650$ km s^{-1}), which were also persistent and pervasive during the current minimum. The first intermediate-speed stream lasted from Day 6 to Day 12 recorded by the OMNI data. The second one started from Day 15 and ended on Day 20. Comparing the simulation results with the observed data, we find

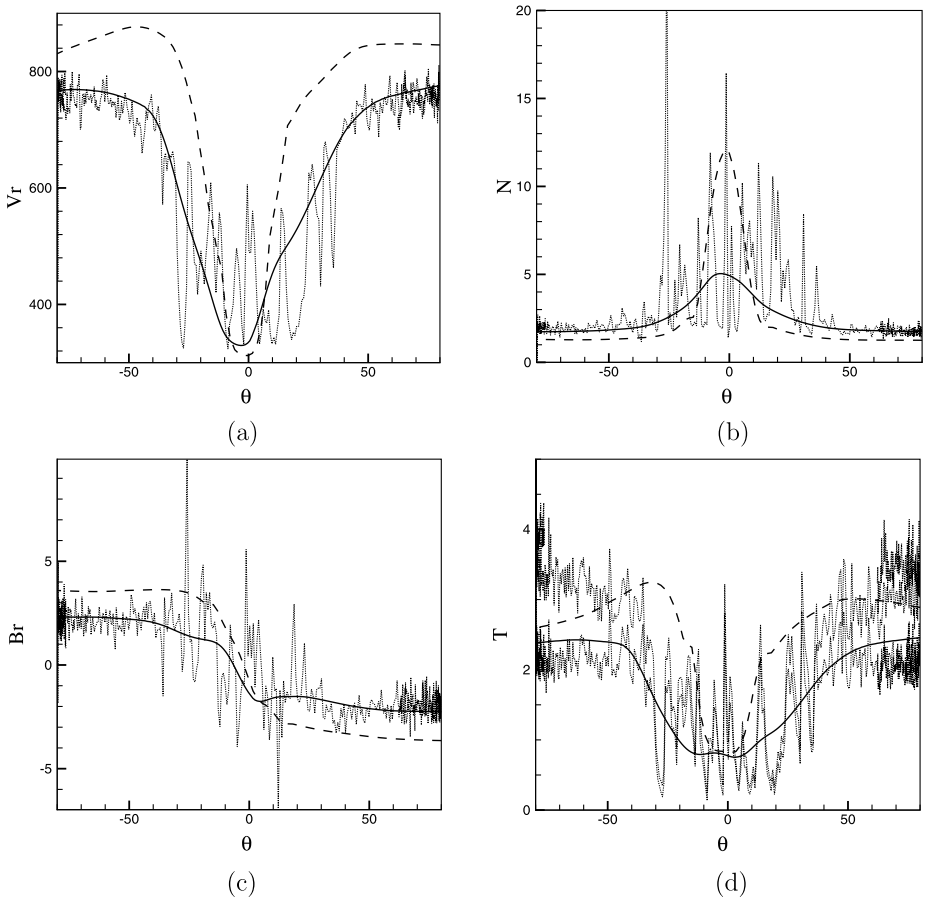

Figure 4 Comparisons between the daily averaged data normalized to 1 AU from *Ulysses* (dotted lines) and the MHD results with the observed photospheric magnetic field of CR 2070 (solid lines). Shown are the latitudinal profiles of (a) radial flow speed v_r in units of km s^{-1}, (b) number density N in units of cm^{-3}, (c) radial magnetic field B_r in units of nT, and (d) temperature T in units of 10^5 K, respectively. The dashed lines represent the MHD results with the strengthened radial polar fields described in Section 3.2.

that the first intermediate-speed stream arrived about one day later than that observed by STEREO-A and about two days later than that observed by STEREO-B, although it is well consistent with the OMNI data. The second one arrived almost at the same time as observed but it persisted a little longer compared to the observation of STEREO-A. However, the simulation misses the third intermediate-speed stream recorded by STEREO-A from Day 21.5 to Day 23. Nevertheless, the MHD model also reproduces the corotating interaction regions (CIRs) which were accompanied by these two intermediate-speed streams and were characteristic of the enhancements of the density, temperature, and magnetic field when the intermediate-speed streams catch up with the front low-speed solar wind. However, the gradients of the solar wind speed associated with CIRs are not as steep as those from all the observations. Generally speaking, the model roughly captures the polarity of the magnetic field during the selected time interval, although the field strength is a bit lower compared with the observations. Finally, it should be mentioned that both the simulation results and the

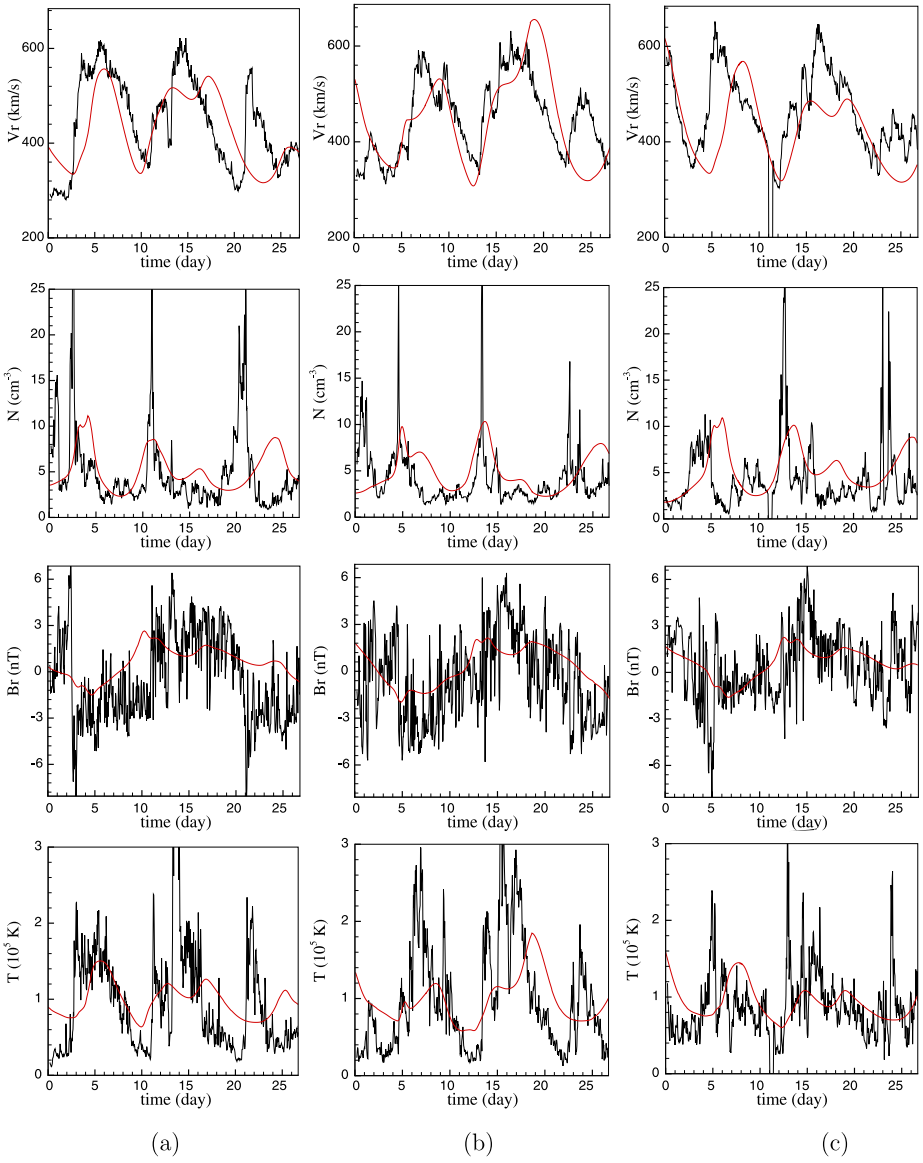

Figure 5 Comparisons between the MHD results and the 1-h averaged data from the (a) STEREO-A, (b) OMNI, and (c) STEREO-B near 1 AU for the radial flow speed v_r, number density N, radial magnetic field B_r, and temperature T.

observations reveal the decreases of density and magnetic field in this period as compared with the results during CR 1911 from Figure 18 of Feng *et al.* (2010).

3.2. Results with the Strengthened Polar Fields

The polar magnetic fields play an important role in controlling the structures of the corona and the solar wind, particularly the topology of the HCS and the distributions of the solar

wind speed. Pneuman, Hansen, and Hansen (1978) found that the discrepancy between the MNL and the brightness maxima of the K-coronameter measurements decreased as the polar fields were strengthened. Hoeksema, Wilcox, and Scherrer (1983) discovered that contributions of the polar field should be included in the calculation of the MNL by the potential field method. In addition, the ratio of the dipole component to the quadrupole component determines the structure of the HCS. Sanderson *et al.* (2003) pointed out that even close to solar maximum when the ratio was high, the HCS was relatively flat although still highly inclined. Furthermore, Wang and Sheeley (1990) and Arge and Pizzo (2000) established reliable formulae between the expansion factor f_s of the magnetic flux tube, which was associated with the polar fields, and the velocity of solar wind at 1 AU. Suzuki (2006) derived a better relationship of $v \propto B/f_s$, where B is the photospheric magnetic field intensity.

Recently, it has been pointed out in the literature that the weak polar fields possibly led to the peculiarities during the current minimum. Tokumaru *et al.* (2009) considered that the weak dipole component was essential to account for the increase of the low-latitude open flux and the non-dipolar solar wind structure in the SCs 23/24 minimum. Tokumaru, Kojima, and Fujiki (2010) showed that the areas of the high-speed solar wind were positively correlated with polar fields and those of the slow wind were inversely correlated. Also, Luhmann *et al.* (2009) found that the weaker polar fields could lead to more prominent low- to mid-latitude coronal holes and therefore stronger high-intermediate-speed wind streams near the ecliptic plane.

We also noted that Wang, Robbrecht, and Sheeley (2009) showed that the photospheric flux density increases with latitude at least as steeply as $\sin^7\theta$, which was consistent with the results from Svalgaard, Duvall, and Scherrer (1978) and Petrie and Patrikeeva (2009). Therefore, following Wang, Robbrecht, and Sheeley (2009), we added an axisymmetric flux distribution of the form $B_r = -6\sin^7\theta$ to the observed photospheric field to include the effects of the polar fields on the solar coronal and interplanetary structures. The added magnetic flux is mainly concentrated in latitudes poleward of 60° and roughly increases the polar fields by two-thirds. In the following, we will concisely display the MHD results with strengthened polar fields.

Figure 6 displays the contour maps of the simulated B_r at 1 R_s and B_r, v_r, and N at 2.5 R_s with the strengthened polar fields, where the black lines denote the MNLs and the orange lines represent the derived boundaries of coronal holes. Figure 6(a) shows that the median of the equatorward boundaries for both northern and southern PCHs is about at $\theta = 60°$ and the northern PCH extends to about $\theta = 0°$ at $\phi = 280°$.

Figure 6(a) shows that the median of the equatorward boundaries for both northern and southern PCHs is about $\theta = 60°$, while the median is about $\theta = 63°$ in the simulated results with the observed polar magnetic field as shown in Figure 1(a). In addition, the northern PCH extends to $\theta = 0°$ at $\phi = 280°$. Comparing with Figure 1(a), we can find that the strengthened polar fields have enlarged the latitudinal widths of PCHs, have eliminated both the isolated MLCH and the southern extended PCH, and have made shrunk the northern extended PCH. Figures 6(b), (c), and (d) exhibit that the addition of the axisymmetric flux has flattened the MNL toward the solar equator and compressed the band of slow solar wind surrounding the MNL. The maximum latitudinal deviation of the MNL from the equator has turned out not to be exceeding 15°. The densities around the MNL, where the slow solar wind pervades, are nearly twice those with the observed polar magnetic field.

Figures 7(a) and (b) show the derived pB images from the simulation with the strengthened polar fields on the meridional planes at $\phi = 270° - 90°$ and $\phi = 120° - 300°$ from 1.15

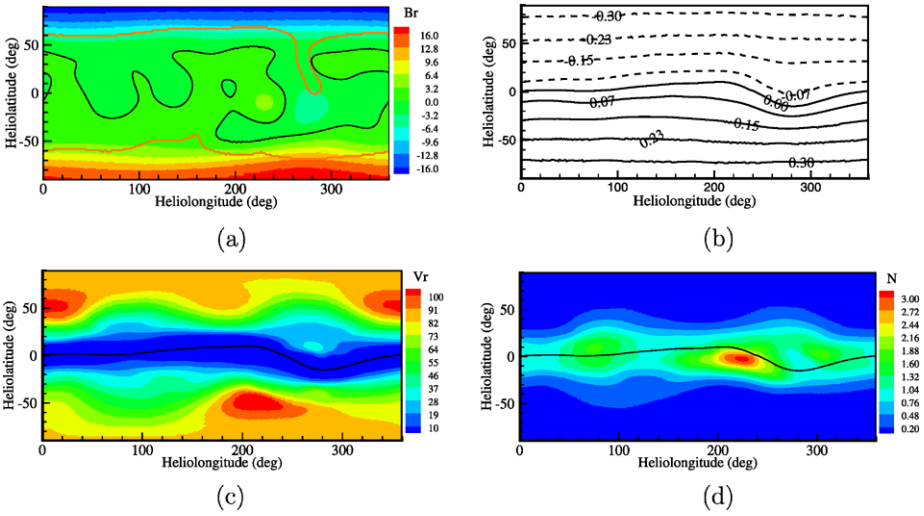

Figure 6 The results of simulations with the strengthened polar fields, showing the distributions of (a) B_r at 1 R_s and (b) B_r, (c) v_r, and (d) N at 2.5 R_s, respectively. In these maps the black lines denote the MNLs and the orange lines represent the derived boundaries of coronal holes. The units of the physical quantities are identical with those in Figure 1.

to 6 R_s. Figures 7(c) and (d) show the corresponding magnetic field topologies from 1 to 6 R_s, in which the color contours represent B_r on the solar surface and the red lines denote MNL. Combination of this figure and Figure 2 reveals that the multiple streamers have been replaced with a single streamer for the case of the strengthened polar fields. The single streamer has the closed magnetic field lines closer to the solar surface, covers smaller latitude ranges and is less inclined toward the solar equator. At the same time, the polar open-field regions occupy a larger area and have a stronger radial magnetic field. Since a significant portion of the magnetic fluxes at high latitudes is connected to the opposite-polarity flux at middle or low latitudes, the weak polar fields in the current minimum lead to the concurrence of smaller PCHs, larger extended PCHs, and the MLCH, which makes the MNL more complex. The addition of axisymmetric polar flux has little effect on the distributions of photospheric magnetic field at middle or low latitudes. Therefore, only a relatively small portion of the polar fields is linked to the opposite-polarity fluxes at middle or low latitudes. As a result, more polar magnetic field flux reaches out to the heliosphere and the PCHs span more latitudes compared with the results with the observed photospheric magnetic fields. Meanwhile, the MHD model suggests that the increased axial dipole moment due to the strengthened polar fields flattens the MNL and simplifies the streamer structures, which is in agreement with Wang, Robbrecht, and Sheeley (2009).

Figures 8(a), (b), (c), and (d) give the contours of B_r, v_r, N, and T at 215 R_s, respectively. These figures delineate a new picture different from that with the observed polar magnetic fields shown in Figure 3. The most prominent characteristic is the flat HCS denoted by the black lines. The HCS is nearly coincident with the solar equator and their maximum latitudinal excursion is about 5° at $\phi = 200°$, while the value is about 15° for the case with the observed polar magnetic fields. It should also be noted that the high-speed solar winds originating from the increased PCHs extend equatorward to middle or even low latitudes. As a result, the latitudinal width of the uniform high-speed solar winds has increased from about 45° to 60° in one hemisphere and the corresponding latitudinal width

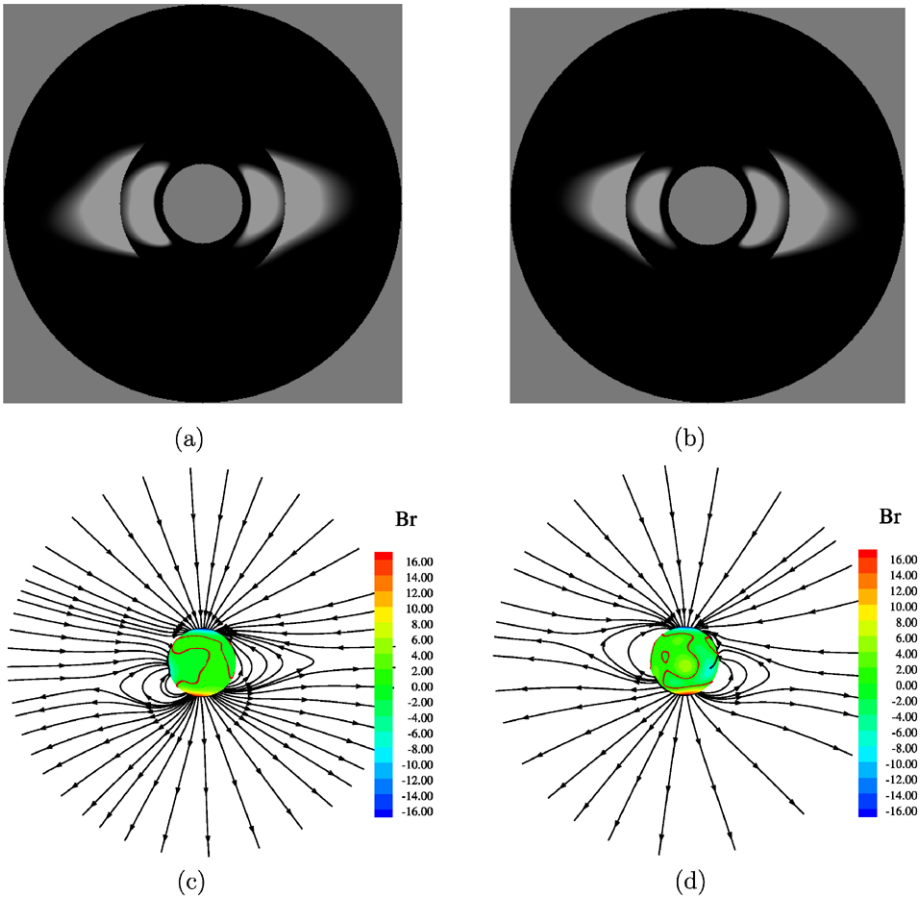

Figure 7 Similar to Figure 2 but only from the MHD results with the strengthened polar fields.

of the SIS solar wind has decreased from about 45° to 30°. Additionally, the strengthened polar fields have eliminated the highlighted feature of two broad intermediate-speed stream near $\phi = 80°$ and $\phi = 220°$ shown in Figure 3(b). The equatorward parts of both regions are now occupied by the low-speed streams and the poleward portions by the high-speed streams.

We have also compared the latitudinal variations of the solar wind parameters obtained from the strengthened polar fields with the measurements from *Ulysses*, which are shown in Figure 4. The comparisons reveal that for the case of the strengthened polar fields, the wider high-speed solar winds carry the enhanced B_r, v_r, and T, and the narrower low-speed solar winds change little except the highly increased density N. Riley *et al.* (2010) found that there was a linear relationship between N and B_r in the high-speed quiescent solar wind observed by *Ulysses*. However, Figure 4 does not present this relationship for the simulations. This is probably attributable to the unchanged mass flux density on the solar surface in the simulation with the strengthened polar magnetic fields, because Wang, Robbrecht, and Sheeley (2009) derived that the mass flux density at the coronal base increased almost linearly with the photospheric field strength basing on interplanetary measurements and photospheric magnetic field observation during 1998 – 2007.

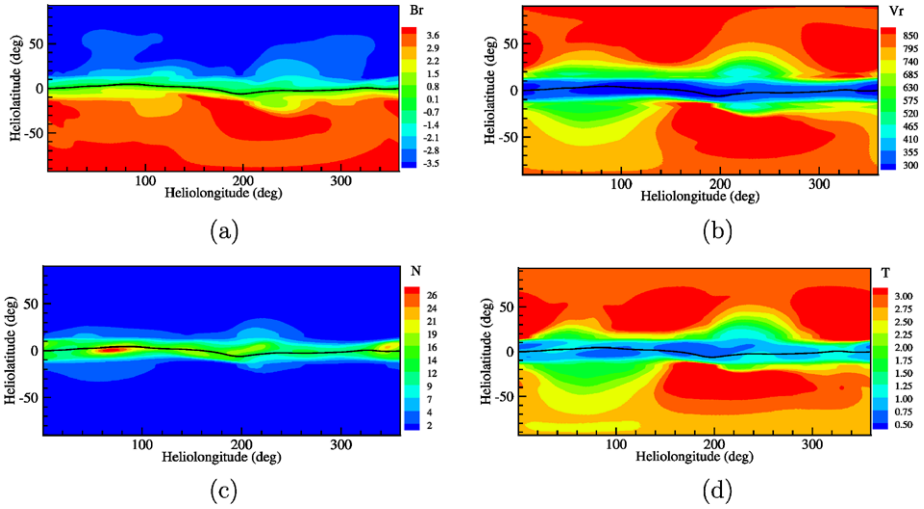

Figure 8 Similar to Figure 3 but with the strengthened polar fields

4. Discussion and Conclusions

In this paper, we have numerically studied the coronal and interplanetary peculiarities during the current minimum with the help of 3D SIP-CESE MHD model. We have selected CR 2070 as the simulated time interval, conducted the simulations and compared the numerical results with the observations from LASCO/C2, *Ulysses*, STEREO and *Wind*/ACE. One simulation was accomplished with the observed photospheric magnetic field as the initial magnetic input and the other with an addition of polar axisymmetric flux to the observed magnetic field.

The first simulation has produced a lot of features near the Sun during the current minimum. The shapes and distributions of both PCHs and extended PCHs from the MHD solution are roughly consistent with STEREO/EUVI observation. The MHD model has also captured the isolated MLCH around $\theta = -15°$ and $\phi = 225°$ but missed the one around $\theta = -25°$ and $\phi = 170°$. Additionally, the simulation results have achieved the 3D structures of the highly inclined, broad, multiple streamers observed by LASCO/C2. The MHD model has revealed that the multiple streamers result from the projection effects on the sky plane of the high-density regions originating from both the helmet streamer and the pseudo-streamer located in different latitudes. The results have exhibited the inconsistency between the streamer belts and the MNL near the Sun due to the presence of the pseudo-streamer as demonstrated by Wang, Sheeley, and Rich (2007).

A great many features observed in the solar wind structures have been reproduced by the simulation with the observed photospheric magnetic field. However, both the HCS and the streamer belt at 215 R_s obtained from the simulation have been shifted southward a few degrees relative to the solar equator, as was suggested by Mursula and Hiltula (2003). The model has also demonstrated the inconsistency of the minimum speed locus with the HCS inferred from the statistical results (Mursula, Hiltula, and Zieger, 2002). The latitudinal width of the high-speed streams is roughly in agreement with the measurements from *Ulysses* during its third fast latitudinal scan but it is smaller than that in its first fast latitudinal scan. In addition, compared with the observations and simulations in the 1996 solar minimum, the high-speed solar wind in our numerical results shows slightly lower speed,

temperature, density and weaker IMF, and so is the solar wind near the solar equator except a little higher speed. We have also noted that the results near the ecliptic plane include the two broad intermediate-speed streams associated with CIRs, which are persistent and pervasive during the current minimum. It should be pointed that the simulated features near the ecliptic plane arrive late by about 1 or 2 days relative to the observations from STEREO.

The simulation with the strengthened polar fields displays completely different coronal and solar wind structures. The simulated results have shown that the relatively large PCHs occupy both poles, the slightly small extended PCH is present at $\phi = 280°$ and the single and narrow streamer of low inclination toward the solar equator covers the region near the solar equator. Similarly, the numerical results at 1 AU have indicated that the uniform high-speed streams prevail in the latitudes poleward of about 30° and carry the enhanced B_r, v_r, and T when compared with the first simulation with the observed polar magnetic field. Near the solar equator, the HCS has been stretched and the band of slow solar wind with high density has pervaded the equatorial regions.

Comparison between both simulations suggests that the weak polar fields play an important role in producing the observed distinct features during the current minimum, such as the slightly small PCHs, the presence of MLCHs, the multiple streamers, the titled and warped HCS, and the relatively long-duration intermediate-speed solar wind near the ecliptic plane. As we know, the famous Maunder minimum (MM) during 1645 – 1715 recorded exceptionally few sunspots (Eddy, 1976; Letfus, 2000). Wang and Sheeley (2003) used the flux transport model to investigate the evolution of the Sun's magnetic dipole moment, polar fields and open flux under the MM conditions and derived that the polar fields during the MM ranged from 0.5 to 2 G. The polar fields in both the 2008 current minimum and the MM have large reductions, although the reduction during the MM is more severe. This similarity and our simulation results may shed some light on the understanding of the state of the background solar wind during the MM. We may infer that the HCS during the MM was probably warped rather than flat in the common solar minima and thus the Earth may have experienced frequent impacts from the intermediate- and high-speed solar streams originating from MLCHs and extending PCHs.

Although the MHD simulations have succeeded in reproducing some observations and provided some insights into the understanding of the special current minimum, further work must be done to more precisely capture the observed coronal and interplanetary features and more deeply recognize the peculiarities and their underlying nature. In fact, there were fewer occurrences of intermediate-speed solar wind observed near the Earth in 2009 (Kataoka and Miyoshi, 2010), although the polar field strength was getting small. Comparative study of the background solar wind in 2008 and 2009 is therefore also worthwhile to create models for comprehensive understanding of the current minimum, which will be a part of our future tasks. Besides, in order to obtain the more realistic results, we should incorporate more observations and more realistic heating mechanisms into the MHD model and assimilate the results from the statistical and empirical models into the future simulations. In addition, numerical researchers should consider more physics in the model, develop more accurate, robust codes and adopt more efficient, high-resolution grids, such as the adaptive mesh refinement grid technology. On the other hand, the coronal MHD models should be coupled with those for lower solar atmospheric layers including the effects of solar dynamo (Charbonneau, 2005; Hoeksema, 2010) operating in the solar convection zone in order for us to better and more deeply perceive how the peculiarities during the current solar minimum are produced and affect the solar and interplanetary phenomena. These efforts will also be helpful to forecast the long-term solar activity and its effects.

Acknowledgements The work is jointly supported by the National Natural Science Foundation of China (41031066, 40921063, 40874091, 40890162, 40904050, 40874077, and 41074122), and the Specialized Research Fund for State Key Laboratories. The numerical calculation has been completed on our SIGMA Cluster computing system. The Wilcox Solar Observatory data used in this study were obtained via the web site http://wso.stanford.edu. The Wilcox Solar Observatory is currently supported by NASA. The MLSO coronagraphs are operated by the High Altitude Observatory, which is sponsored by the National Science Foundation (USA). SOHO is a project of international cooperation between ESA and NASA. The STEREO/SECCHI data are produced by a consortium of NRL (US), LMSAL (US), NASA/GSFC (US), RAL (UK), UBHAM (UK), MPS (Germany), CSL (Belgium), IOTA (France), and IAS (France). We appreciate the SPDF COHOWeb database for helpfully providing data. The OMNI data were obtained from the GSFC/SPDF OMNIWeb interface at http://omniweb.gsfc.nasa.gov. The authors would like to express their sincere thanks to the anonymous reviewer for the invaluable suggestions and grammatical corrections.

References

Abramenko, V., Yurchyshyn, V., Linker, J., Mikić, Z., Luhmann, J., Lee, C.O.: 2010, Low-latitude coronal holes at the minimum of the 23rd solar cycle. *Astrophys. J.* **712**, 813.

Arge, C.N., Pizzo, V.J.: 2000, Improvement in the prediction of solar wind conditions using near-real time solar magnetic field updates. *J. Geophys. Res.* **105**, 10465.

Arge, C.N., Luhmann, J.G., Odstrcil, D., Schrijver, C.J., Li, Y.: 2004, Stream structure and coronal sources of the solar wind during the May 12th, 1997 CME. *J. Atmos. Solar-Terr. Phys.* **66**, 1295.

Bame, S.J., McComas, D.J., Barraclough, B.L., Phillips, J.L., Sofaly, K.J., Chavez, J.C., Goldstein, B.E., Sakurai, R.K.: 1992, The ULYSSES solar wind plasma experiment. *Astron. Astrophys. Suppl.* **92**, 237.

Braginskii, S.I.: 1965, Transport processes in a plasma. *Rev. Plasma Phys.* **1**, 205.

Charbonneau, P.: 2005, Dynamo models of the solar cycle. *Living Rev. Solar Phys.* **2**(2).

Cooper, J.F., King, J.H., Mathews, G.J., McGuire, R.E., Papitashvili, N.E., Parthasarathy, R., Towheed, S.S.: 1995, Internet access to NASA's OMNI and COHO data bases for interplanetary missions. In: *International Cosmic Ray Conference* **4**, 1295.

de Toma, G., Arge, C.N.: 2010, The Sun's magnetic field during the past two minima. In: Maksimovic, M., Issautier, K., Meyer-Vernet, N., Moncuquet, M., Pantellini, F. (eds.) *Twelfth International Solar Wind Conference*, *AIP Conf. Proc.* **1216**, 679.

Delaboudinière, J., Artzner, G.E., Brunaud, J., Gabriel, A.H., Hochedez, J.F., Millier, F., Song, X.Y., Au, B., Dere, K.P., Howard, R.A., Kreplin, R., Michels, D.J., Moses, J.D., Defise, J.M., Jamar, C., Rochus, P., Chauvineau, J.P., Marioge, J.P., Catura, R.C., Lemen, J.R., Shing, L., Stern, R.A., Gurman, J.B., Neupert, W.M., Maucherat, A., Clette, F., Cugnon, P., van Dessel, E.L.: 1995, EIT: Extreme-ultraviolet Imaging Telescope for the SOHO mission. *Solar Phys.* **162**, 291.

Eddy, J.A.: 1976, The Maunder Minimum. *Science* **192**, 1189.

Endeve, E., Leer, E., Holzer, T.E.: 2003, Two-dimensional magnetohydrodynamic models of the solar corona: Mass loss from the streamer belt. *Astrophys. J.* **589**, 1040.

Erdős, G., Balogh, A.: 2010, North-south asymmetry of the location of the heliospheric current sheet revisited. *J. Geophys. Res.* **115**, 1105.

Feng, X., Zhou, Y., Wu, S.T.: 2007, A novel numerical implementation for solar wind modeling by the modified conservation element/solution element method. *Astrophys. J.* **655**, 1110.

Feng, X., Yang, L., Xiang, C., Wu, S.T., Zhou, Y., Zhong, D.: 2010, Three-dimensional solar wind modeling from the Sun to Earth by a SIP-CESE MHD model with a six-component grid. *Astrophys. J.* **723**, 300.

Gibson, S.E., Kozyra, J.U., de Toma, G., Emery, B.A., Onsager, T., Thompson, B.J.: 2009, If the Sun is so quiet, why is the Earth ringing? A comparison of two solar minimum intervals. *J. Geophys. Res.* **114**, 9105.

Hathaway, D.H., Rightmire, L.: 2010, Variations in the Sun's meridional flow over a solar cycle. *Science* **327**, 1350.

Hoeksema, J.T.: 2010, Evolution of the large-scale magnetic field over three solar cycles. In: Kosovichev, A.G., Andrei, A.H., Roelot, J.P. (eds.) *Solar and Stellar Variability: Impact on Earth and Planets*, *IAU Symposium* **264**, 222.

Hoeksema, J.T., Wilcox, J.M., Scherrer, P.H.: 1983, The structure of the heliospheric current sheet – 1978 – 1982. *J. Geophys. Res.* **88**, 9910 – 9918.

Hu, Y.Q., Feng, X.S., Wu, S.T., Song, W.B.: 2008, Three-dimensional MHD modeling of the global corona throughout solar cycle 23. *J. Geophys. Res.* **113**, A03106.

Issautier, K., Le Chat, G., Meyer-Vernet, N., Moncuquet, M., Hoang, S., MacDowall, R.J., McComas, D.J.: 2008, Electron properties of high-speed solar wind from polar coronal holes obtained by Ulysses thermal noise spectroscopy: Not so dense, not so hot. *Geophys. Res. Lett.* **35**, L19101.

Kaiser, M.L., Kucera, T.A., Davila, J.M., St. Cyr, O.C., Guhathakurta, M., Christian, E.: 2008, The STEREO mission: An introduction. *Space Sci. Rev.* **136**, 5.
Kataoka, R., Miyoshi, Y.: 2010, Why are relativistic electrons persistently quiet at geosynchronous orbit in 2009? *Space Weather* **8**, 8002.
Kataoka, R., Ebisuzaki, T., Kusano, K., Shiota, D., Inoue, S., Yamamoto, T.T., Tokumaru, M.: 2009, Three-dimensional MHD modeling of the solar wind structures associated with 13 December 2006 coronal mass ejection. *J. Geophys. Res.* **114**, 10102.
Kirk, M.S., Pesnell, W.D.: 2009, Automated detection of polar coronal holes in the EUV. *Bull. Am. Astron. Soc.* **41**, 834.
Kleimann, J., Kopp, A., Fichtner, H., Grauer, R.: 2009, A novel code for numerical 3-D MHD studies of CME expansion. *Ann. Geophys.* **27**, 989.
Lee, C.O., Luhmann, J.G., Zhao, X.P., Liu, Y., Riley, P., Arge, C.N., Russell, C.T., de Pater, I.: 2009, Effects of the weak polar fields of solar cycle 23: Investigation using OMNI for the STEREO mission period. *Solar Phys.* **256**, 345.
Lepping, R.P., Acũna, M.H., Burlaga, L.F., Farrell, W.M., Slavin, J.A., Schatten, K.H., Mariani, F., Ness, N.F., Neubauer, F.M., Whang, Y.C., Byrnes, J.B., Kennon, R.S., Panetta, P.V., Scheifele, J., Worley, E.M.: 1995, The wind magnetic field investigation. *Space Sci. Rev.* **71**, 207.
Lepri, S.T., Antiochos, S.K., Riley, P., Zhao, L., Zurbuchen, T.H.: 2008, Comparison of heliospheric in situ data with the quasi-steady solar wind models. *Astrophys. J.* **674**, 1158.
Letfus, V.: 2000, Sunspot and auroral activity during Maunder Minimum. *Solar Phys.* **197**, 203.
Linker, J.A., Mikić, Z., Biesecker, D.A., Forsyth, R.J., Gibson, S.E., Lazarus, A.J., Lecinski, A., Riley, P., Szabo, A., Thompson, B.J.: 1999, Magnetohydrodynamic modeling of the solar corona during Whole Sun Month. *J. Geophys. Res.* **104**, 9809.
Luhmann, J.G., Li, Y., Arge, C.N., Gazis, P.R., Ulrich, R.: 2002, Solar cycle changes in coronal holes and space weather cycles. *J. Geophys. Res.* **107**, 1154.
Luhmann, J.G., Lee, C.O., Li, Y., Arge, C.N., Galvin, A.B., Simunac, K., Russell, C.T., Howard, R.A., Petrie, G.: 2009, Solar wind sources in the late declining phase of cycle 23: Effects of the weak solar polar field on high speed streams. *Solar Phys.* **256**, 285.
McComas, D.J., Elliott, H.A., Gosling, J.T., Skoug, R.M.: 2006, Ulysses observations of very different heliospheric structure during the declining phase of solar activity cycle 23. *Geophys. Res. Lett.* **33**, L09102.
McComas, D.J., Ebert, R.W., Elliott, H.A., Goldstein, B.E., Gosling, J.T., Schwadron, N.A., Skoug, R.M.: 2008, Weaker solar wind from the polar coronal holes and the whole Sun. *Geophys. Res. Lett.* **35**, L18103.
Morgan, H., Habbal, S.R., Woo, R.: 2006, The depiction of coronal structure in white-light images. *Solar Phys.* **236**, 263.
Mursula, K., Hiltula, T.: 2003, Bashful ballerina: southward shifted heliospheric current sheet. *Geophys. Res. Lett.* **30**(22), 2-1.
Mursula, K., Hiltula, T., Zieger, B.: 2002, Latitudinal gradients of solar wind speed around the ecliptic: Systematic displacement of the streamer belt. *Geophys. Res. Lett.* **29**(15), 28-1.
Nakamizo, A., Tanaka, T., Kubo, Y., Kamei, S., Shimazu, H., Shinagawa, H.: 2009, Development of the 3-D MHD model of the solar corona-solar wind combining system. *J. Geophys. Res.* **114**, 7109.
Owens, M.J., Arge, C.N., Spence, H.E., Pembroke, A.: 2005, An event-based approach to validating solar wind speed predictions: High-speed enhancements in the Wang–Sheeley–Arge model. *J. Geophys. Res.* **110**, 12105.
Petrie, G.J.D., Patrikeeva, I.: 2009, A comparative study of magnetic fields in the solar photosphere and chromosphere at equatorial and polar latitudes. *Astrophys. J.* **699**, 871.
Pneuman, G.W., Hansen, S.F., Hansen, R.T.: 1978, On the reality of potential magnetic fields in the solar corona. *Solar Phys.* **59**, 313.
Riley, P., Linker, J.A., Mikić, Z., Lionello, R., Ledvina, S.A., Luhmann, J.G.: 2006, A comparison between global solar magnetohydrodynamic and potential field source surface model results. *Astrophys. J.* **653**, 1510.
Riley, P., Mikic, Z., Lionello, R., Linker, J.A., Schwadron, N.A., McComas, D.J.: 2010, On the relationship between coronal heating, magnetic flux, and the density of the solar wind. *J. Geophys. Res.* **115**, 6104.
Sanderson, T.R., Appourchaux, T., Hoeksema, J.T., Harvey, K.L.: 2003, Observations of the Sun's magnetic field during the recent solar maximum. *J. Geophys. Res.* **108**, 1035.
Schatten, K.: 2005, Fair space weather for solar cycle 24. *Geophys. Res. Lett.* **32**, L21106.
Smith, E.J., Balogh, A.: 2008, Decrease in heliospheric magnetic flux in this solar minimum: recent Ulysses magnetic field observations. *Geophys. Res. Lett.* **35**, L22103.
Stone, E.C., Frandsen, A.M., Mewaldt, R.A., Christian, E.R., Margolies, D., Ormes, J.F., Snow, F.: 1998, The Advanced Composition Explorer. *Space Sci. Rev.* **86**, 1.
Suzuki, T.K.: 2006, Forecasting solar wind speeds. *Astrophys. J.* **640**, L75.

Svalgaard, L., Duvall, T.L. Jr., Scherrer, P.H.: 1978, The strength of the Sun's polar fields. *Solar Phys.* **58**, 225.

Tokumaru, M., Kojima, M., Fujiki, K.: 2010, Solar cycle evolution of the solar wind speed distribution from 1985 to 2008. *J. Geophys. Res.* **115**, 4102.

Tokumaru, M., Kojima, M., Fujiki, K., Hayashi, K.: 2009, Non-dipolar solar wind structure observed in the cycle 23/24 minimum. *Geophys. Res. Lett.* **36**, L09101.

Usmanov, A.V., Goldstein, M.L., Besser, B.P., Fritzer, J.M.: 2000, A global MHD solar wind model with WKB Alfvén waves: Comparison with Ulysses data. *J. Geophys. Res.* **105**, 12675.

Wang, Y., Sheeley, N.R. Jr.: 1990, Solar wind speed and coronal flux-tube expansion. *Astrophys. J.* **355**, 726.

Wang, Y.-M., Sheeley, N.R. Jr.: 2003, Modeling the Sun's large-scale magnetic field during the Maunder Minimum. *Astrophys. J.* **591**(2), 1248.

Wang, Y., Lean, J., Sheeley, N.R. Jr.: 2000, The long-term variation of the Sun's open magnetic flux. *Geophys. Res. Lett.* **27**, 505.

Wang, Y., Robbrecht, E., Sheeley, J.N.R.: 2009, On the weakening of the polar magnetic fields during solar cycle 23. *Astrophys. J.* **707**, 1372.

Wang, Y., Sheeley, N.R. Jr., Rich, N.B.: 2007, Coronal pseudostreamers. *Astrophys. J.* **658**, 1340.

Wang, Y., Sheeley, N.R. Jr., Howard, R.A., Kraemer, J.R., Rich, N.B., Andrews, M.D., Brueckner, G.E., Dere, K.P., Koomen, M.J., Korendyke, C.M., Michels, D.J., Moses, J.D., Paswaters, S.E., Socker, D.G., Wang, D., Lamy, P.L., Llebaria, A., Vibert, D., Schwenn, R., Simnett, G.M.: 1997, Origin and evolution of coronal streamer structure during the 1996 minimum activity phase. *Astrophys. J.* **485**, 875.

Wenzel, K.P., Marsden, R.G., Page, D.E., Smith, E.J.: 1992, The ULYSSES mission. *Astron. Astrophys. Suppl.* **92**, 207.

Zhao, X.P., Hoeksema, J.T., Liu, Y., Scherrer, P.H.: 2006, Success rate of predicting the heliospheric magnetic field polarity with Michelson Doppler Imager (MDI) synoptic charts. *J. Geophys. Res.* **111**, A10108.